



Article

Internal Temperature Estimation for Lithium-Ion Cells Based on a Layered Electro-Thermal Equivalent Circuit Model

Wei Shi ^{1,2}, Wei Li ^{2,3} and Shusheng Xiong ^{1,2,3,*}¹ College of Energy Engineering, Zhejiang University, Hangzhou 310027, China; shiw@zju.edu.cn² Provincial Key Laboratory of New Energy Vehicles Thermal Management, Longquan 323700, China; liweisail@zju.edu.cn³ Longquan Industrial Innovation Research Institute, Longquan 323700, China

* Correspondence: xiongss@zju.edu.cn

Abstract: In the domain of Battery Management System (BMS) research, the precise acquisition and estimation of internal temperature distribution within lithium-ion cells is a significant challenge. The commercial viability precludes the use of internal temperature sensors, and existing methodologies for online estimation of internal temperatures under various electrical loads are constrained by computational limitations and model accuracy. This study presents a layered electro-thermal equivalent circuit model (LETECM), developed by integrating a layered second-order fractional equivalent circuit model with a layered thermal equivalent circuit model. A lithium-ion battery divided into three layers was employed to illustrate the development of this LETECM. The model's precision was validated against a 3D Newman Finite Element Model (3DNFEM), constructed using actual battery parameters. Given that the thermal gradient inside the battery is usually more pronounced under high load conditions, a 10C direct current discharge for 60 s followed by a rest period of 240 s was adopted as the test condition in the simulation. The results indicate that at the end of the DC discharge, the temperature difference between the inner layer and the surface of the battery was the largest and the maximum temperature difference predicted by the LETECM was 3.58 °C, while the 3DNFEM exhibited a temperature difference of 3.74 °C. The trends in each layer temperature and battery surface temperature obtained by the two models are highly consistent. The proposed model offers computational efficiency and maintains notable accuracy, suggesting its potential integration into BMS for real-time online applications. This advancement could provide critical internal temperature data for refining battery charging and discharging performance assessments and lifespan predictions, thereby optimizing battery management strategies.



Citation: Shi, W.; Li, W.; Xiong, S. Internal Temperature Estimation for Lithium-Ion Cells Based on a Layered Electro-Thermal Equivalent Circuit Model. *Batteries* **2024**, *10*, 406. <https://doi.org/10.3390/batteries10110406>

Academic Editor: Harry E. Hoster

Received: 16 August 2024

Revised: 9 September 2024

Accepted: 30 September 2024

Published: 18 November 2024



Copyright: © 2024 by the authors. Licensee MDPI, Basel, Switzerland. This article is an open access article distributed under the terms and conditions of the Creative Commons Attribution (CC BY) license (<https://creativecommons.org/licenses/by/4.0/>).

1. Introduction

Lithium batteries, as a crucial energy source, possess notable advantages such as high efficiency and environmental friendliness, particularly in mobile power applications. They eliminate issues associated with internal combustion engines like vibration, low efficiency, excessive weight, and noise, and they do not produce greenhouse gasses or toxic emissions resulting from incomplete fossil fuel combustion [1,2]. Additionally, lithium batteries demonstrate faster response times to dynamic loads compared to internal combustion engines [3]. Considering performance and environmental impacts related to hydrocarbon emissions, electric power systems are poised to dominate the transportation sector. Indeed, lithium ion and lithium polymer technologies are already extensively utilized in commercial vehicles, small commercial drones [4–6], and short-distance yachts.

The increase in battery power and size exacerbates thermal gradients within battery cells, particularly significant for high-performance applications like electric vehicles operating in harsh environments. The temperature distribution within batteries, characterized

by spatio-temporal coupling, is crucial for battery health, as excessive internal temperature differences can diminish discharge capacity and shorten battery life [7–10]. Extreme temperatures can lead to safety hazards, including thermal runaway [11]. Experiments on 18,650 cylindrical batteries at a 3C discharge rate exhibited internal to surface temperature differences of approximately 2.5 °C under natural convection and 5 °C under forced convection [12]. A 10 °C temperature difference was observed in 26,650 cylindrical batteries during a 6C discharge [13]. Pouch-cell batteries have shown that internal thermal gradients can accelerate degradation by threefold [14]. Compared to pouch-cells, cylindrical cells present inferior heat dissipation capabilities, likely resulting in larger thermal gradients [15]. This confirms the presence of internal temperature gradients in lithium batteries, which, under high load, can exceed the safe temperature differences within battery packs [16].

Advanced BMS should have core functions such as rapid heat dissipation, uniform temperature field regulation, and early detection of thermal runaway. These thermal management strategies necessitate the development and employment of a distributed thermal model for lithium-ion batteries to furnish precise temperature field predictions. While surface temperature measurement is relatively straightforward, internal temperature sensing using in-cell thermocouples, although valuable for research [17], lacks practicality for commercial battery production due to concerns over thermocouple chemical stability and increased costs.

In recent years, numerous studies have attempted to circumvent complex physical constraints by employing purely data-driven approaches for the intelligent modeling of battery thermal processes [18–20]. When sufficient training data are available, the models established exhibit commendable predictive accuracy. However, as the proportion of training data decreases, the performance of these models on the test set gradually deteriorates. Moreover, model updates necessitate time-consuming retraining using accumulated historical data, rendering them unsuitable for industrial applications requiring rapid responses. Improved methods such as temporal correlation-based incremental KL (TCI-KL), sliding window-based KL (SW-KL), and spatial correlation-based incremental KL (SCI-KL) [21–24] have enhanced computational efficiency to varying degrees. Nevertheless, they still rely on a retraining update mechanism using a batch of data. Concurrently, data-driven modeling methods, due to their significant dependence on input/output data, mandate the deployment of a multitude of sensors within the spatial domain, a requirement that might prove challenging to fulfill in practical scenarios.

The electrochemical-thermal model, grounded in first principles, meticulously delineates the reciprocal influence between the electrochemical and thermal processes inherent to lithium-ion batteries. Possessing the utmost physical relevance, these models facilitate the observation of alterations in physically quantifiable elements that elude measurement during operational states. In the wake of the seminal modeling endeavors on lithium-ion battery electrochemical systems by the Newman group, a myriad of mathematical methodologies have been employed to scrutinize the dynamic attributes of battery systems [25,26]. The electrochemical-thermal model encompasses a vast array of information, customarily necessitating the employment of multiple coupled partial differential equations for comprehensive description. The intricate model architecture and the surfeit of model parameters substantially constrain the practical application. Contrastingly, the electrothermal equivalent circuit model (ECM) offers well-defined physical implications and straightforward mathematical expressions. Typical electrical equivalent circuit models include the resistor model (Rint model) [27], the first-order resistor-capacitor (RC) model (also referred to as the Thevenin model) [28], the second-order RC model (i.e., the dual polarization model) [29], and the PNGV model [30]. These ECMS feature direct and explicit relationships between parameters and generally involve a comparatively lesser quantity. Consequently, only ECMS have been implemented in BMS for online real-time computation.

Until now, limited by the computational cost and model accuracy, there are still a lack of tools to effectively estimate the internal temperature distribution within batteries under a wide range of electrical loads. This paper introduces the LETECM to address these

issues. The LETECM is presented in Section 2. In Section 3, the accuracy of the LETECM is evaluated using a 3D Newman electrochemical-thermal finite element model.

2. Model Description

2.1. Layered Second-Order Fractional Equivalent Circuit Model

The research methods and conclusions in this paper are not limited to types of lithium-ion batteries, but in this paper, cylindrical lithium-ion batteries are taken as an example. In the existing research, there are methods to evaluate the internal temperature distribution of batteries by using the heat transfer model with a layered structure, but there is no electrical equivalent circuit model with a layered structure.

In recent years, fractional-order equivalent circuit models have been increasingly adopted [31–33]. The existing literature has demonstrated that fractional-order models can more accurately reproduce the time–frequency characteristics of batteries. Figure 1 depicts the second-order fractional equivalent circuit model used in this paper.

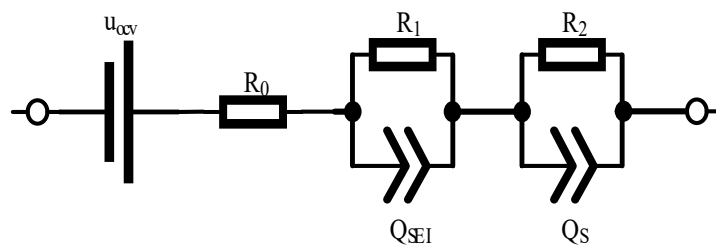


Figure 1. Second-order fractional equivalent circuit model of lithium-ion battery.

Given the limited contribution of the ultra-high frequency component to the real part of battery impedance, this study excludes the inductive element from the equivalent circuit. The resistance R_0 represents the transfer impedance of lithium ions and electrons through the electrolyte, porous separator, conductors, and active material particles. The resistance R_1 and constant phase element Q_{SEI} characterize the resistive properties and constant phase behavior associated with the solid electrolyte interface film on the surface of the active material particles. The resistance R_2 and constant phase element Q_S describe the solid-state diffusion of lithium ions within the active material, the liquid-state diffusion in the electrolytic solution, and the transfer impedance at the solid–liquid interface of the active material, including the electric double layer effect and the constant phase element arising from its uneven surface [34].

Based on the equivalent circuit model depicted in Figure 1, the proposed layered equivalent circuit model is shown in Figure 2. Lithium-ion batteries are composed of multiple composite layers that are wound together, and the relationship between these winding layers can be considered to be parallel connections within the equivalent circuit. During the theoretical derivation, a specific number of layers is not designated, and it is represented by the letter n .

According to Kirchhoff's current law, the current i_{bat} in Figure 2 can be expressed as:

$$i_{bat} = \sum_{i=1}^n i_i = \sum_{i=1}^n \frac{u_{OCV} - u_o}{Z_i} \quad (1)$$

where Z_i represents the impedance of branch i . The relationship between voltage and current can be expressed as:

$$\frac{u_{OCV} - u_o(s)}{i(s)} = \left(\sum_{i=1}^n \left(R_{0i} + \frac{1}{\frac{1}{R_{1i}} + Q_{SEIi}s^{\alpha_i}} + \frac{1}{\frac{1}{R_{2i}} + Q_{Si}s^{\beta_i}} \right)^{-1} \right)^{-1} \quad (2)$$

where α and β is the fractional order.

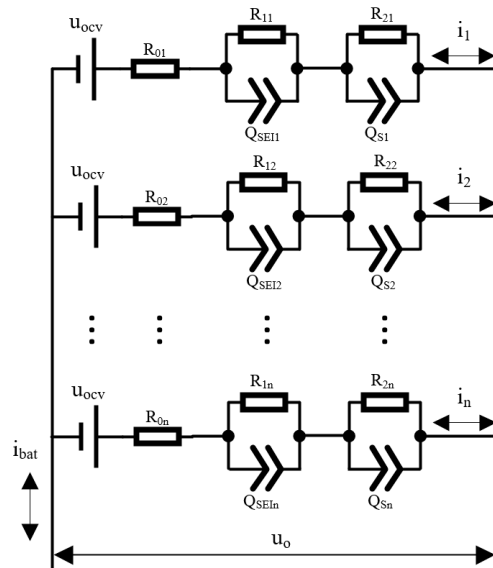


Figure 2. Layered second-order fractional equivalent circuit model of lithium-ion battery.

Equation (2) represents the mathematical formulation of the layered fractional equivalent circuit model for lithium-ion batteries. This equation allows for the computation of the battery's impedance spectrum. Subsequently, the real part of this impedance spectrum can be derived. The heat generation power of the battery can then be calculated, which serves as the input to the thermal model of the battery. In conjunction with this, the LETECM of the battery is established. As inferred from the aforementioned formula, an increase in the number of layers results in a higher order for the model and a corresponding rise in the number of parameters to be identified. An excessive number of layers can result in a substantial computational load and protracted calculation times for the model. Therefore, the selection of the number of model layers should strike a balance between accuracy and computational load.

In this study, a three-layer model is employed. For cylindrical batteries, this model partially accounts for the non-uniform radial parameter distribution while overlooking the axial parameter variations. Given the spiral configuration of the anode, cathode, separator, and current collector within the battery, which results in high thermal conductivity along the axial direction, such an approximation is justified. Concurrently, to minimize the number of model parameters and ensure that the extension length of each layer is consistent, the parameters for each layer are solely coupled with temperature and are not associated with geometric characteristics. Following the arrangement of the transfer function for the three-layer model using Equation (2), we obtain:

$$\frac{u_{OCV} - u_o(s)}{i(s)} = \left(\sum_{i=1}^3 \left(\frac{a_{1i}s^{\alpha_i + \beta_i} + a_{2i}s^{\alpha_i} + a_{3i}s^{\beta_i} + a_{4i}}{b_{1i}s^{\alpha_i + \beta_i} + b_{2i}s^{\alpha_i} + b_{3i}s^{\beta_i} + 1} \right)^{-1} \right)^{-1}. \quad (3)$$

The expansion formula of each parameter in the above formula is as follows:

$$\left\{ \begin{array}{l} a_{1i} = R_{0i}R_{1i}R_{2i}Q_{SEIi}Q_{Si} \\ a_{2i} = R_{0i}R_{1i}Q_{SEIi} + R_{1i}R_{2i}Q_{SEIi} \\ a_{3i} = R_{0i}R_{2i}Q_{Si} + R_{1i}R_{2i}Q_{Si} \\ a_{4i} = R_{0i} + R_{1i} + R_{2i} \\ b_{1i} = R_{1i}R_{2i}Q_{SEIi}Q_{Si} \\ b_{2i} = R_{1i}Q_{SEIi} \\ b_{3i} = R_{2i}Q_{Si} \end{array} \right. \quad (4)$$

The model encompasses a total of 21 parameters that require identification. Furthermore, the inability to measure currents within different regions of the battery cell presents challenges for parameter identification. Therefore, in practical parameter identification, it is possible to proceed using a lumped parameter approach. The equivalent circuit model incorporates the open-circuit voltage U_{OCV} . Its functional relationship with the state of charge (SOC) can be described using the Nernst model [35].

2.2. Layered Thermal Equivalent Circuit Model

In this study, a layered thermal equivalent circuit model is introduced to assess the internal temperature distribution of cylindrical batteries. The model subdivides the interior of the battery, and with an increased number of layers, the model more accurately represents the actual temperature distribution within the battery. However, a higher number of layers also necessitates greater computational power. Given that heat transfer characteristics can be analogized and simplified through electrical behavior, transforming the heat transfer model into an equivalent circuit model allows for the direct formulation of differential equations using Kirchhoff's current or voltage laws. This facilitates the computation of the dynamic temperature distribution within the battery.

The steel shell of the battery has a thickness of approximately 0.2 mm, and while its radial temperature distribution can be disregarded, its heat capacity cannot be overlooked and is considered to be a lumped parameter. The equivalent circuit model for an $n + 1$ layer, constructed on this premise, is illustrated in Figure 3. The temperature of each layer is expressed by U_{ax} ($x = 1, 2, \dots, n$), and the shell temperature is expressed by U_s . The material's equivalent thermal conductivity and the thermal resistance between layers are denoted by R_{ax} ($x = 1, 2, \dots, n$). The contact thermal resistance between the outermost material and the shell is represented by R_{ns} . The equivalent heat transfer resistance due to convection and radiation between the shell and the surrounding environment is denoted by R_{sf} . The heat capacity of each layer within the battery is defined as C_{ax} ($x = 1, 2, \dots, n$), and the heat generation power is analogous to a current source with current values of I_{ax} ($x = 1, 2, \dots, n$). The external environment of the battery is likened to a voltage source with U_f .

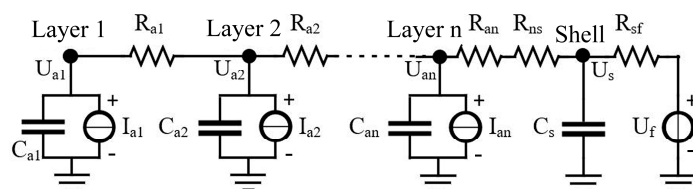


Figure 3. Layered thermal equivalent circuit model of lithium-ion battery.

Consistent with the example in Section 2.1, the number of layers is 3. In accordance with Kirchhoff's circuit laws, the nodal current equations can be formulated at the intersections of circuits representing each layer, with electrical parameters substituted for the aforementioned thermal parameters. The three layers and shell thermal equivalent circuit model can be expressed by the following equations.

$$\text{Layer 1} \quad m_1 c_{a1} \frac{dT_{a1}}{dt} = 2\lambda A_{12} \frac{T_{a2} - T_{a1}}{\delta_1 + \delta_2} + P_{a1} \quad (5)$$

$$\text{Layer 2} \quad m_2 c_{a2} \frac{dT_{a2}}{dt} = 2\lambda A_{12} \frac{T_{a1} - T_{a2}}{\delta_1 + \delta_2} + 2\lambda A_{23} \frac{T_{a3} - T_{a2}}{\delta_2 + \delta_3} + P_{a2} \quad (6)$$

$$\text{Layer 3} \quad m_3 c_{a3} \frac{dT_{a3}}{dt} = \frac{T_s - T_{a3}}{\frac{\delta_3}{2\lambda A_{3s}} + R_{3s}} + 2\lambda A_{32} \frac{T_{a2} - T_{a3}}{\delta_3 + \delta_2} + P_{a3} \quad (7)$$

$$\text{Shell} \quad m_s c_s \frac{dT_s}{dt} = \frac{T_{a3} - T_s}{\frac{\delta_3}{2\lambda A_{3s}} + R_{3s}} + \frac{T_f - T_s}{R_{sf}} \quad (8)$$

where m_x is the x -th layer quality, T_{ax} is the x -th layer temperature, T_s is the shell temperature, T_f is the ambient temperature, P_{ax} is the heat generation power of x -th layer, A is the area between layers, δ is the thickness of layer, and λ is the thermal conductivity ($x = 1, 2, \dots, n$).

The battery is divided into three layers, and the length of each layer's winding structure is the same, so the volume of each layer is the same. In this case, both A and δ in the equation set can be directly calculated based on the dimensions of the battery. Other parameters such as heat capacity and thermal conductivity can be derived from the material properties of the battery.

2.3. Layered Electro-Thermal Equivalent Circuit Model

Using the layered second-order fractional equivalent circuit model and layered thermal equivalent circuit model in the above chapter, the LETECM as shown in Figure 4 is constructed.

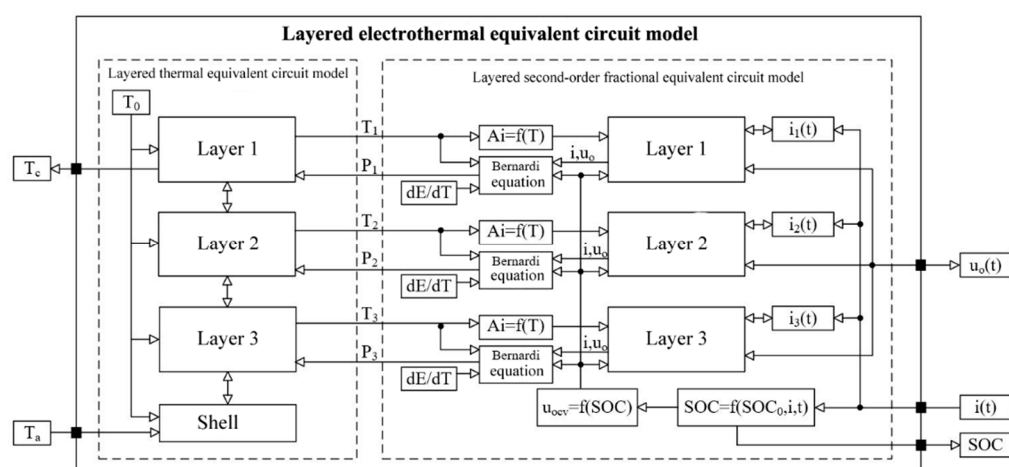


Figure 4. Schematic diagram of layered electro-thermal equivalent circuit model.

Firstly, the parameters of the equivalent circuit model are determined based on the initial temperature T_0 and initial SOC₀ of the battery through a lookup table. In conjunction with the u_{OCV} , which is also looked up, and the input current $i(t)$, the polarization voltage can be computed within the equivalent circuit model and, subsequently, the heat generation power P_i for each layer. The open-circuit voltage temperature coefficient reflects the reversible chemical reaction heat of the battery, which is defined as dE/dT . The temperature coefficient of the open circuit voltage is a function of SOC and temperature [36]. Then, using the ambient temperature T_a , the heat generation power of each layer, and the initial temperature of the battery, the temperature rise in each layer is calculated in the heat transfer model. This information is immediately fed back to the electrical model to update its parameters for the next iteration of heat generation power calculation. Through this iterative process, dynamic information regarding the core temperature T_c and the temperature difference between the surface and the core can be obtained. Similarly, the SOC(t) and $u_O(t)$ of the battery can be calculated.

3. Simulation Verification and Discussion

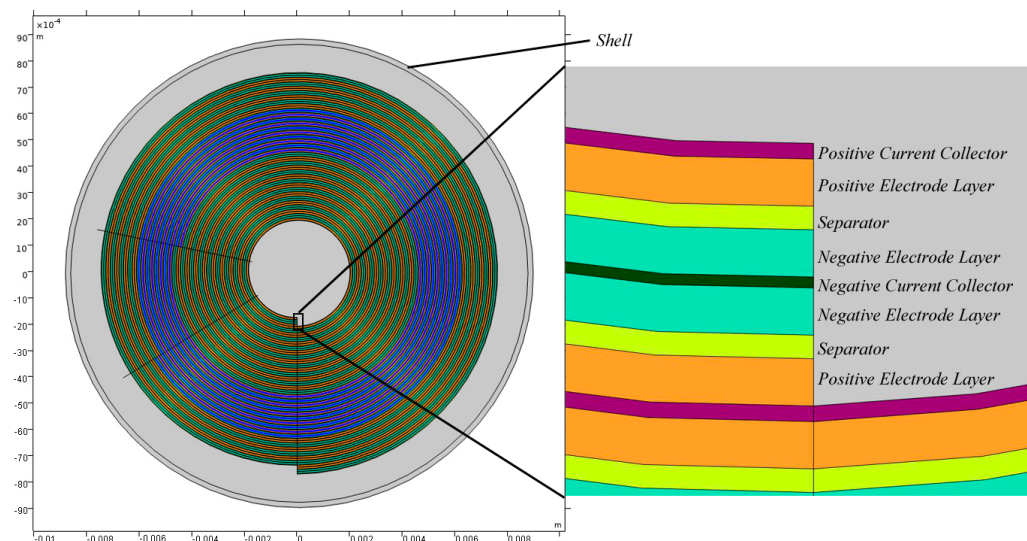
3.1. Finite Element Model Based on 3D Newman

Without compromising the integrity of the battery, it is impossible to directly ascertain its internal temperature. Furthermore, the stratified current density remains immeasurable through experimental means. Consequently, to validate the precision of the LETECM, this study employs specific battery specimens (whose parameters are delineated in Table 1) to construct a finite element model grounded on the 3D Newman model, necessitating substantial computational resources.

Table 1. Parameter list of battery samples.

Parameter	Value	Unit
Type	INR1865025P	-
Positive/negative electrode material	LFP/Graphite	-
Rated capacity	2500	mAh
Nominal voltage	3.6	V
Charge/discharge cut-off voltage	4.2/2.5	V
Maximum charging current	4	A
Maximum continuous discharge rate	12	C
Quality	48	g

This model is a comprehensive 3D Newman model, inclusive of an additional dimension that describes the intercalation and diffusion of lithium particles at the granular scale. Moreover, the model takes into account the heat generation and thermal conduction processes caused by Ohmic polarization, electrochemical polarization, and more, involving components such as electrodes, separators, and current collectors. A composite sheet is rolled according to Figure 5. The thickness of the composite sheet is 3.34×10^{-4} m. It consists of individual layers of a positive current collector, a positive electrode, a diaphragm, a negative electrode, a negative current collector, a negative electrode, a diaphragm, and a positive electrode from bottom to top [37,38]. The whole winding structure is placed in a steel casing filled with electrolytes. Using the composite sheet of the battery as a unit and following the principle of equal volume, the interior of the battery is divided into three layers. In polar coordinates, the calculated angle of the inner layer is from 0 to 16.565π , the middle layer from 16.565π to 26.325π , and the outer layer from 26.325π to 34π . The highlighted middle section in Figure 5 represents the middle layer.

**Figure 5.** Battery model and diagram of battery divided into three layers.

3.2. Parameter Identification for LETECM

Electrochemical impedance spectroscopy is a crucial method for revealing the internal dynamics of electrochemical devices. A small sinusoidal variation is applied to the potential of the working electrode, and the resulting current is analyzed in the frequency domain. The real and imaginary parts of the impedance provide information about the battery's kinetics and mass transfer properties, as well as capacitive characteristics. The Nyquist plot is the most common way to present impedance experiment results, with the real

part (resistance) plotted on the x -axis and the imaginary part (reactance) plotted on the y -axis [39]. In the finite element model, an AC amplitude of 5 mV is set with a frequency range of 0.01–1 kHz. The initial temperatures are set to 25 °C, 35 °C, 45 °C, and 55 °C. Impedance data at different SOC levels are obtained by setting the initial concentration of positive and negative material particles to achieve an SOC lower limit of 5% and an upper limit of 95%, with a 15% SOC interval.

The impedance data mentioned above are employed to conduct parameter identification on the LETECM. The parameter fitting outcomes for various temperatures and SOCs are organized, resulting in seven parameters for the model as shown in the figure below.

R_0 characterizes the transfer impedance of lithium ions and electrons through the electrolyte, porous separators, conductors, active material particles, etc. As shown in Figure 6. The temperature range in the simulation, 25–55 degrees Celsius, represents the normal operating temperatures for lithium-ion batteries, and it can be observed from this figure that R_0 tends to decrease gradually with increasing temperature. R_0 does not vary significantly with SOC.

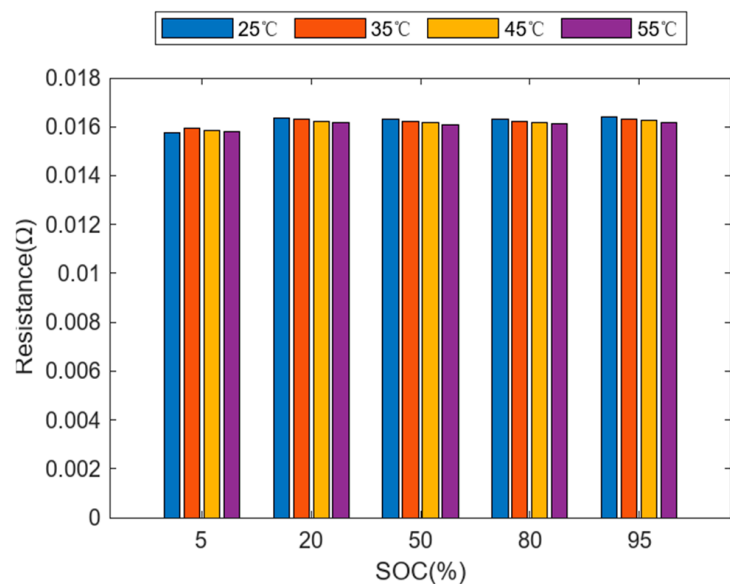


Figure 6. Identification result of LETECM: R_0 .

In the high-frequency region, the resistance (R_1) corresponding to the surface SEI film of active material particles and the constant phase angle element (Q_{SEI}) are identified, where Q_{SEI} is represented by the capacitive reactance T_1 and the fractional order P_1 . As shown in Figure 7. It can be observed that the capacitive reactance and fractional order vary significantly at low SOCs and they are more affected by temperature under low SOC conditions.

In the mid-to-low frequency region, it is characterized by the resistance (R_2) and the constant phase element (Q_S). This portion of the resistance consists of the transfer impedance of charges at the solid–liquid interface of active materials, as well as the solid-state diffusion impedance within the active materials and the liquid-phase diffusion impedance in the electrolyte solution. As shown in Figure 8. When the SOC is 5%, this impedance primarily occurs at the cathode, resulting in a significantly large impedance. The double-layer effect causes T_2 to become extremely small.

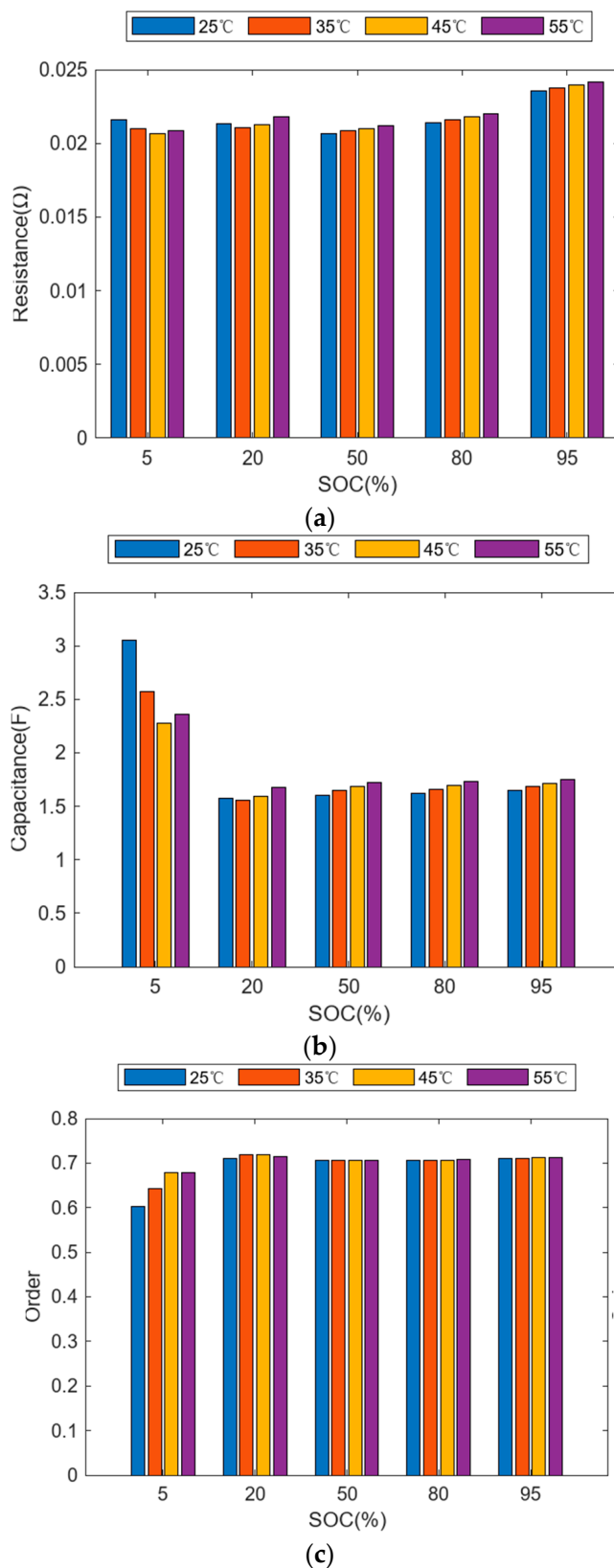


Figure 7. Identification result of LETECM: (a) R_1 , Q_{SEI} include parameters (b) T_1 and (c) P_1 .

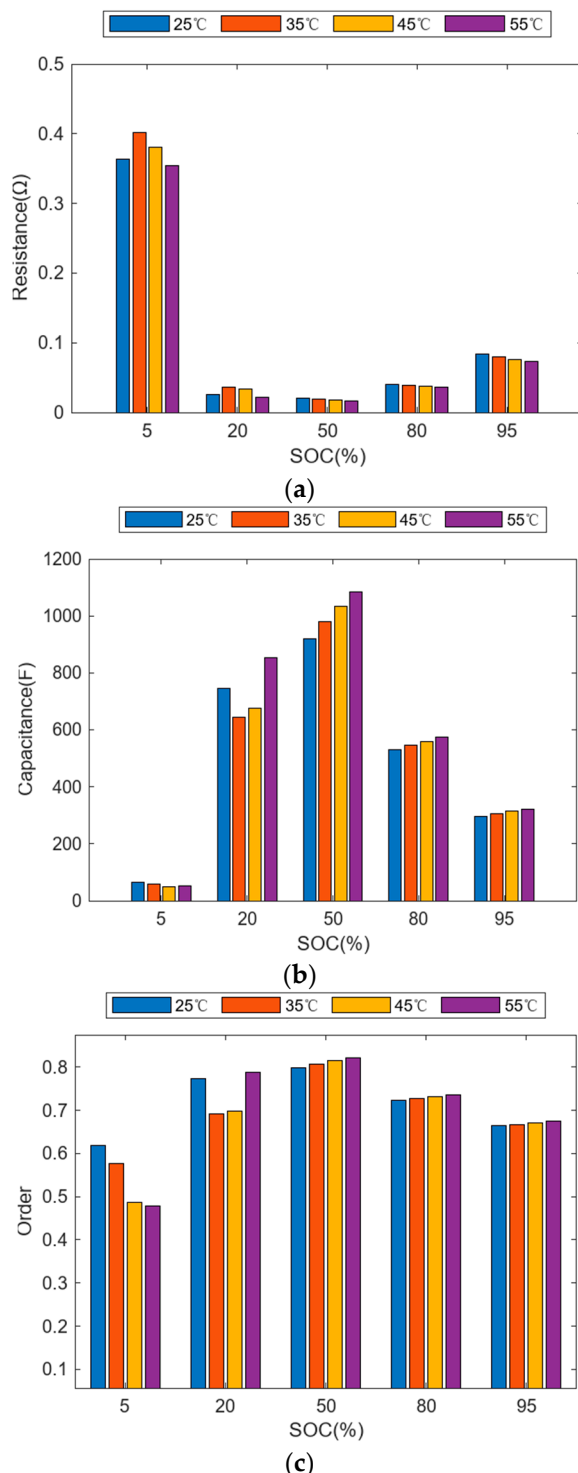


Figure 8. Identification result of LETECM: (a) R_2 , Q_s include parameters (b) T_2 and (c) P_2 .

3.3. Verification of the LETECM

To verify the validity and precision of the model, a 10C (25 A) discharge simulation is conducted using the finite element model and the thermal-electrical model. The initial values and experimental conditions for both models are set identically. Upon completion of the simulation, a comparison is made of the temperature changes over time in the inner, middle, outer layers, and surface of the cell core, as well as the current changes over time in the inner, middle, and outer layers.

During the 10C discharge simulation, the starting SOC is set to 95%, with continuous discharge for 60 s and a total simulation duration of 300 s. The curves showing the changes in temperature and maximum temperature difference over time in the inner, middle, outer layers, and surface for both models are presented in the figure below.

The temperature rise and fall trends in the two models are very consistent. As shown in Figure 9. At the end of DC discharge, the temperature difference between the inner layer and the surface of the battery is the largest. The maximum temperature difference for the finite element model is $3.74\text{ }^{\circ}\text{C}$, while that for the thermal-electrical model is $3.58\text{ }^{\circ}\text{C}$. Throughout the simulation process, the greatest difference occurs at the end of the greatest discrepancy between the two models occurs at the end of the simulation, with a difference of $0.4\text{ }^{\circ}\text{C}$.

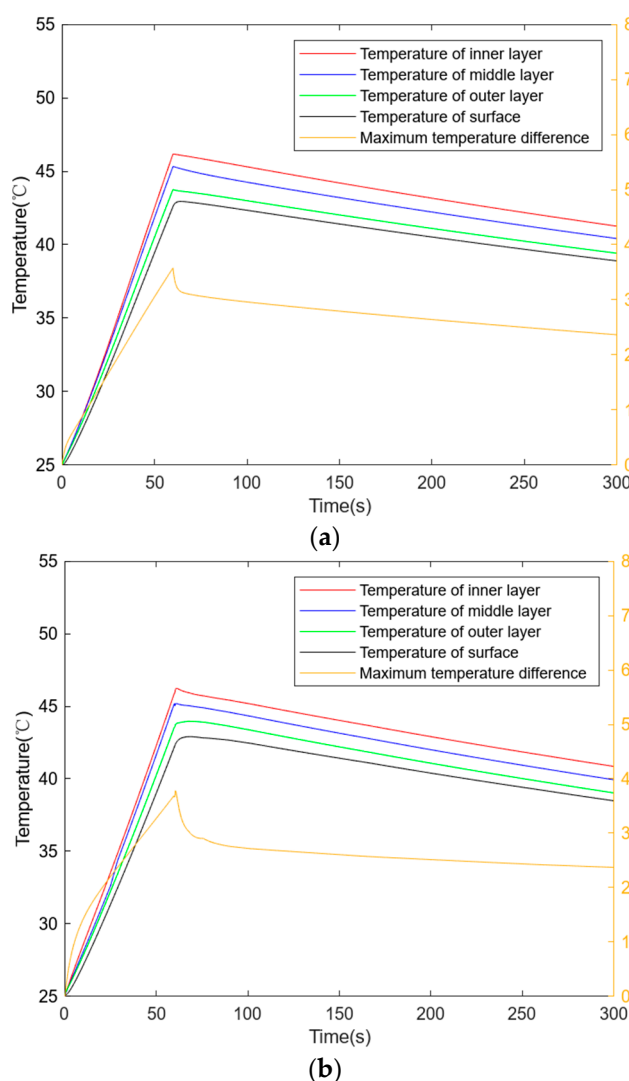


Figure 9. Curve of inner layer temperature, middle layer temperature, outer layer temperature, surface temperature and maximum temperature difference: (a) LETECM, (b) 3DNFEM.

The variation curves of current over time in the inner, middle, and outer layers for both models are shown in the figure below (inner, middle, and outer layers).

In the LETECM, the battery is numerically divided into three equal parts. Therefore, the current in the three layers is equal at the start. In the 3DNFEM, the battery is geometrically divided. The geometry is trisected based on the length integral of the spiral curve. Then, the rotation angles of the equidistant points in the polar coordinate system are calculated. The current calculated by angular integration is not strictly equal. As shown in Figure 10. The initial current of the inner layer and the outer layer differs by 0.01 A. As

the simulation progresses, the influence of temperature on physical parameters causes the current difference between the three layers to increase. From the figure above, it can be seen that the current change trends in the two models are consistent. At the maximum temperature difference, under the LETECM, the current difference in the three layers is 0.008 A. In the 3DNFEM, excluding the initial difference, the current difference caused by temperature is 0.009 A.

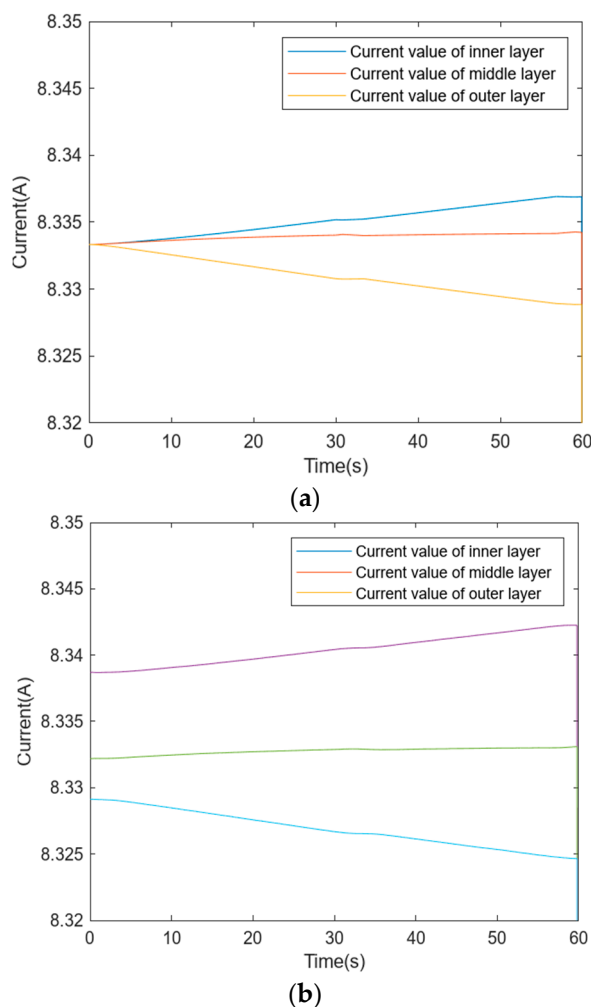


Figure 10. Curve of inner layer current, middle layer current and outer layer current: (a) LETECM, (b) 3DNFEM.

4. Conclusions

This paper utilizes a computationally inexpensive layered electro-thermal equivalent circuit model for estimating the internal temperature of cylindrical lithium-ion batteries. The battery was divided into three equal volume layers in terms of size, and a 10C continuous DC discharge simulation was performed. The temperature trends in each layer and the surface temperature of the battery obtained from the LETECM and 3DNFEM are very consistent. These prediction results demonstrate good accuracy at a lower computational cost, indicating that the LETECM could potentially be deployed in BMS for online real-time operation. This advancement could provide critical internal temperature data for refining battery charging and discharging performance assessments and lifespan predictions, thereby optimizing battery management strategies.

The model parameters are stored in the form of a parameter map that varies with temperature and SOC in this paper. The fractional order is not sensitive to temperature and SOC, which allows for further simplification of the model to conserve resources. As

controller computational power increases, the model can be conveniently expanded to more layers. Consequently, more data on the internal temperature distribution of the battery can be obtained. It is important to note that the model presented in this paper is specifically applicable to cylindrical lithium iron phosphate batteries. Should the model be extended to other types of cylindrical lithium-ion batteries, adjustments to the equivalent circuit model are necessary according to the battery type and its impedance spectral characteristics. If the model is to be applied to prismatic or other shaped lithium-ion batteries, corresponding modifications in the geometric layering of the model are required.

Author Contributions: Methodology, W.S.; Software, W.L.; Validation, W.L.; Data curation, W.S.; Writing—original draft, W.S.; Writing—review & editing, S.X. All authors have read and agreed to the published version of the manuscript.

Funding: This research was funded by Zhejiang Province Spearhead and Leading Goose Research and Development Key Program, grant number 2023C01239.

Data Availability Statement: The original contributions presented in the study are included in the article, further inquiries can be directed to the corresponding author.

Conflicts of Interest: The authors declare no conflict of interest.

Nomenclature

Symbol	Abbreviation
U_{OCV}	open circuit voltage of the battery (V)
R_0	the transfer impedance (Ω)
R_1	the resistive properties associated with the solid electrolyte interface film on the surface of the active material particles (Ω)
R_2	the transfer impedance at the solid–liquid interface of the active material (Ω)
Q_{SEI}	the constant phase behavior associated with the Solid Electrolyte Interface film on the surface of the active material particles (F)
Q_S	the constant phase element arising from its uneven surface (F)
n	number of layers
i_{bat}	battery current (A)
i_i	($i = 1, 2, \dots, n$) current in the i -th layer (A)
Z_i	($i = 1, 2, \dots, n$) impedance of branch i (Ω)
s	Laplace operator
α	fractional order
β	fractional order
R_{ax}	($x = 1, 2, \dots, n$) thermal resistance between x layer and $x + 1$ layer (K/W)
R_{ns}	thermal resistance between the n layer and the shell (K/W)
R_{sf}	thermal resistance between the shell and the surrounding environment (K/W)
C_{ax}	($x = 1, 2, \dots, n$) heat capacity of x -th layer within the battery (J/(kg·K))
C_s	heat capacity of shell (J/(kg·K))
I_{ax}	($x = 1, 2, \dots, n$) the heat generation power is analogous to a current source with current values of I_{ax} (W)
U_{ax}	($x = 1, 2, \dots, n$) the x -th layer temperature (K)
U_f	the ambient temperature (K)
U_s	the shell temperature (K)
m_x	($x = 1, 2, \dots, n$) the x -th layer quality (kg)
T_{ax}	($x = 1, 2, \dots, n$) the x -th layer temperature (K)
T_f	the ambient temperature (K)
T_s	the shell temperature (K)
P_{ax}	($x = 1, 2, \dots, n$) the heat generation power of x -th layer (W)
A	area between layers (m^2)
δ	thickness of layer (m)
λ	thermal conductivity (W/(m·K))

References

1. E, J.; Liu, G.; Zhang, Z.; Han, D.; Chen, J.; Wei, K.; Gong, J.; Yin, Z. Effect analysis on cold starting performance enhancement of a diesel engine fueled with biodiesel fuel based on an improved thermodynamic model. *Appl. Energy* **2019**, *243*, 321–335. [[CrossRef](#)]
2. Shu, J.; Fu, J.; Zhao, D.; Liu, J.; Ma, Y.; Deng, B.; Zeng, D.; Liu, J.; Zhang, Y. Numerical investigation on the effects of valve timing on in-cylinder flow, combustion and emission performance of a diesel ignition natural gas engine through computational fluid dynamics. *Energy Convers. Manag.* **2019**, *198*, 111786. [[CrossRef](#)]
3. Lei, T.; Yang, Z.; Lin, Z.; Zhang, X. State of art on energy management strategy for hybrid-powered unmanned aerial vehicle. *Chin. J. Aeronaut.* **2019**, *32*, 1488–1503. [[CrossRef](#)]
4. Donateo, T.; Ficarella, A.; Spedicato, L.; Arista, A.; Ferraro, M. A new approach to calculating endurance in electric flight and comparing fuel cells and batteries. *Appl. Energy* **2017**, *187*, 807–819. [[CrossRef](#)]
5. Yang, C.; Moon, S.; Kim, Y. A fuel cell/battery hybrid power system for an unmanned aerial vehicle. *J. Mech. Sci. Technol.* **2016**, *30*, 2379–2385. [[CrossRef](#)]
6. Verstraete, D.; Gong, A.; Lu, D.D.C.; Palmer, J.L. Experimental investigation of the role of the battery in the AeroStack hybrid, fuel-cell-based propulsion system for small unmanned aircraft systems. *Int. J. Hydrogen Energy* **2015**, *40*, 1598–1606. [[CrossRef](#)]
7. Wang, Y.; Zhang, X.; Chen, Z. Low temperature preheating techniques for Lithiumion batteries: Recent advances and future challenges. *Appl. Energy* **2022**, *313*, 118832. [[CrossRef](#)]
8. Raijmakers, L.H.J.; Danilov, D.L.; Eichel, R.A.; Notten, P.H.L. A review on various temperature-indication methods for Li-ion batteries. *Appl. Energy* **2019**, *240*, 918–945. [[CrossRef](#)]
9. Ruan, H.; Jiang, J.; Sun, B.; Su, X.; He, X.; Zhao, K. An optimal internal-heating strategy for lithium-ion batteries at low temperature considering both heating time and lifetime reduction. *Appl. Energy* **2019**, *256*, 113797. [[CrossRef](#)]
10. Zhu, J.; Knapp, M.; Darma, M.S.D.; Fang, Q.; Wang, X.; Dai, H.; Wei, X.; Ehrenberg, H. An improved electro-thermal battery model complemented by current dependent parameters for vehicular low temperature application. *Appl. Energy* **2019**, *248*, 149–161. [[CrossRef](#)]
11. Feng, X.; He, X.; Ouyang, M.; Lu, L.; Wu, P.; Kulp, C.; Prasser, S. Thermal runaway propagation model for designing a safer battery pack with 25Ah LiNixCoyMnzO₂ large format lithium ion battery. *Appl. Energy* **2015**, *154*, 74–91. [[CrossRef](#)]
12. Zhang, G.; Cao, L.; Ge, S. Insitu measurement of radial temperature distributions in cylindrical li-ion cells. *J. Electrochem. Soc.* **2014**, *161*, A1499. [[CrossRef](#)]
13. Forgez, C.; Do, D.V.; Friedrich, G.; Morcrette, M.; Delacourt, C. Thermal modeling of a cylindrical lifepo4/graphite lithium-ion battery. *J. Power Sources* **2010**, *195*, 2961–2968. [[CrossRef](#)]
14. Hunt, I.A.; Zhao, Y.; Patel, Y.; Offer, J. Surface cooling causes accelerated degradation compared to tab cooling for lithium-ion pouch cells. *J. Electrochem. Soc.* **2016**, *163*, A1846–A1852. [[CrossRef](#)]
15. Waldmann, T.; Bisle, G.; Hogg, B.-I.; Stumpf, S.; Danzer, M.A.; Kasper, M.; Axmann, P.; Wohlfahrt-Mehrens, M. Influence of cell design on temperatures and temperature gradients in lithium-ion cells: An in operando study. *J. Electrochem. Soc.* **2015**, *162*, A921–A927. [[CrossRef](#)]
16. Liu, H.; Wei, Z.; He, W.; Zhao, J. Thermal issues about li-ion batteries and recent progress in battery thermal management systems: A review. *Energy Convers. Manag.* **2017**, *150*, 304–330. [[CrossRef](#)]
17. Fleming, J.; Amietszajew, T.; Charmet, J.; Roberts, A.J.; Greenwood, D.; Bhagat, R. The design and impact of in-situ and operando thermal sensing for smart energy storage. *J. Energy Storage* **2019**, *22*, 36–43. [[CrossRef](#)]
18. Zhu, S.; He, C.; Zhao, N.; Sha, J. Data-driven analysis on thermal efects and temperature changes of lithium-ion battery. *J. Power Sources* **2021**, *482*, 228983. [[CrossRef](#)]
19. Liu, Z.; Li, H.X. Extreme learning machine based spatiotemporal modeling of lithium-ion battery thermal dynamics. *J. Power Sources* **2015**, *277*, 228–238. [[CrossRef](#)]
20. Chen, L.Q.; Li, H.X.; Yang, H.D. Dimension embedded basis function for spatiotemporal modeling of distributed parameter system. *IEEE Trans. Ind. Inform.* **2019**, *16*, 5846–5854. [[CrossRef](#)]
21. Wang, Z.; Li, H.X. Incremental spatiotemporal learning for online modeling of distributed parameter systems. *IEEE Trans. Syst. Man Cybern. Syst.* **2018**, *49*, 2612–2622. [[CrossRef](#)]
22. Wang, B.C.; Li, H.X. A sliding window based dynamic spatiotemporal modeling for distributed parameter systems with time-dependent boundary conditions. *IEEE Trans. Ind. Inform.* **2018**, *15*, 2044–2053. [[CrossRef](#)]
23. Wang, B.C.; Li, H.X.; Yang, H.D. Spatial correlation-based incremental learning for spatiotemporal modeling of battery thermal process. *IEEE Trans. Ind. Inform.* **2019**, *16*, 2885–2893. [[CrossRef](#)]
24. Li, S.; Patel, A.N.; Zhang, C.; Amietszajew, T.; Kirkaldy, N.; Offer, G.J.; Marinescu, M. Internal temperature estimation for lithium-ion batteries through distributed equivalent circuit network model. *J. Power Sources* **2024**, *611*, 234701. [[CrossRef](#)]
25. Chiew, J.; Chin, C.S.; Toh, W.D.; Gao, Z.; Jia, J.; Zhang, C.Z. A pseudo three-dimensional electrochemical-thermal model of a cylindrical lifepo4/graphite battery. *Appl. Therm. Eng.* **2019**, *147*, 450–463. [[CrossRef](#)]
26. Wang, D.; Huang, H.; Tang, Z.; Zhang, Q.; Yang, B.; Zhang, B. A lithium-ion battery electrochemical-thermal model for a wide temperature range applications. *Electrochim. Acta* **2020**, *362*, 137118. [[CrossRef](#)]
27. Wu, M.; Qin, L.; Wu, G. State of power estimation of power lithium-ion battery based on an equivalent circuit model. *J. Energy Storage* **2022**, *51*, 104538. [[CrossRef](#)]

28. Wang, C.; Xu, M.; Zhang, Q.; Feng, J.; Jiang, R.; Wei, Y.; Liu, Y. Parameters identification of thevenin model for lithium-ion batteries using self-adaptive particle swarm optimization differential evolution algorithm to estimate state of charge. *J. Energy Storage* **2021**, *44*, 103244. [[CrossRef](#)]
29. Zheng, X.; Zhagn, Z. State of charge estimation at different temperatures based on dynamic thermal model for lithium-ion batteries. *J. Energy Storage* **2022**, *48*, 104011. [[CrossRef](#)]
30. Geng, Y.; Pang, H.; Liu, X. State-of-charge estimation for lithium-ion battery based on pngv model and particle filter algorithm. *J. Power Electron.* **2022**, *22*, 1154–1164. [[CrossRef](#)]
31. Liu, S.; Cui, N.; Li, Y.; Zhang, C. Modeling and state of charge estimation of lithium-ion battery based on theory of fractional order for electric vehicle. *Trans. China Electrotech. Soc.* **2017**, *32*, 189–195.
32. Ge, H. Alternating Current Preheating and Fast Charging of Lithium-Ion Batteries with Lithium Plating Prevention at Low Temperatures. Ph.D. Thesis, Tsinghua University, Beijing, China, 2017.
33. Shang, Y. Optimization Design and Implementation of State Estimation and Balancing Management System for Lithium-Ion Batteries in Electric Vehicles. Ph.D. Thesis, Shangdong University, Jinan, China, 2017.
34. Run, H. Optimal Heating and Charging Methods for Lithium-Ion Batteries Under the Low-Temperature Environment. Ph.D. Thesis, Beijing Jiaotong University, Beijing, China, 2019.
35. Micea, M.V.; Ungurean, L.; CaRstoiu, G.N.; Groza, V. Online state-of-health sssessment for battery management systems. *IEEE Trans. Instrum. Meas.* **2011**, *60*, 1997–2006. [[CrossRef](#)]
36. Özdemir, T.; Amini, A.; Ekici, Ö.; Koksl, M. Experimental assessment of the lumped lithium-ion battery model. *E3S Web Conf.* **2019**, *128*, 1022. [[CrossRef](#)]
37. Yao, X.; Pecht, M. Tab Design and Failures in Cylindrical Li-ion Batteries. *IEEE Access* **2019**, *7*, 24082–24095. [[CrossRef](#)]
38. Doyle, M.; Newman, J.; Gozdz, A.S.; Schmutz, C.N.; Tarascon, J.M. Comparison of Modeling Predictions with Experimental Data from Plastic Lithium Ion Cells. *J. Electrochem. Soc.* **1996**, *143*, 1890–1903. [[CrossRef](#)]
39. Bard, A.J.; Faulkner, L.R. *Electrochemical Methods: Fundamentals and Applications*, 2nd ed.; Wiley: New York, NY, USA, 2020.

Disclaimer/Publisher's Note: The statements, opinions and data contained in all publications are solely those of the individual author(s) and contributor(s) and not of MDPI and/or the editor(s). MDPI and/or the editor(s) disclaim responsibility for any injury to people or property resulting from any ideas, methods, instructions or products referred to in the content.